Remote Sens. **2015**, *7*, 8323-8347; doi:10.3390/rs70708323

OPEN ACCESS

remote sensing

ISSN 2072-4292

www.mdpi.com/journal/remotesensing

Article

StaMPS Improvement for Deformation Analysis in Mountainous Regions: Implications for the Damavand Volcano and Mosha Fault in Alborz

Sanaz Vajedian [1,*], Mahdi Motagh [2,1] and Faramarz Nilfouroushan [3]

[1] Department of Surveying and Geomatics Engineering, University of Tehran, Tehran 14395-515, Iran

[2] GFZ German Research Center for Geosciences, D-14473 Potsdam, Germany; E-Mail: motagh@gfz-potsdam.de

[3] Department of Earth Sciences, Uppsala University, SE 75236 Uppsala, Sweden; E-Mail: faramarz.nilfouroushan@geo.uu.se

* Author to whom correspondence should be addressed; E-Mail: vajedian@ut.ac.ir; Tel.: +98-21-8800-8841; Fax: +98-21-8800-8837.

Academic Editors: Richard Gloaguen and Prasad S. Thenkabail

Received: 17 March 2015 / Accepted: 9 June 2015 / Published: 25 June 2015

Abstract: Interferometric Synthetic Aperture Radar (InSAR) capability to detect slow deformation over terrain areas is limited by temporal decorrelation, geometric decorrelation and atmospheric artefacts. Multitemporal InSAR methods such as Persistent Scatterer (PS-InSAR) and Small Baseline Subset (SBAS) have been developed to deal with various aspects of decorrelation and atmospheric problems affecting InSAR observations. Nevertheless, the applicability of both PS-InSAR and SBAS in mountainous regions is still challenging. Correct phase unwrapping in both methods is hampered due to geometric decorrelation in particular when using C-band SAR data for deformation analysis. In this paper, we build upon the SBAS method implemented in StaMPS software and improved the technique, here called ISBAS, to assess tectonic and volcanic deformation in the center of the Alborz Mountains in Iran using both Envisat and ALOS SAR data. We modify several aspects within the chain of the processing including: filtering prior to phase unwrapping, topographic correction within three-dimensional phase unwrapping, reducing the atmospheric noise with the help of additional GPS data, and removing the ramp caused by ionosphere turbulence and/or orbit errors to better estimate crustal deformation in this tectonically active region. Topographic correction is done within the three-dimensional unwrapping in order to improve the phase unwrapping process, which is in contrast to

previous methods in which DEM error is estimated before/after phase unwrapping. Our experiments show that our improved SBAS approach is able to better characterize the tectonic and volcanic deformation in the center of the Alborz region than the classical SBAS. In particular, Damavand volcano shows an average uplift rate of about 3 mm/year in the year 2003–2010. The Mosha fault illustrates left-lateral motion that could be explained with a fault that is locked up to 17–18 km depths and slips with 2–4 mm/year below that depth.

Keywords: InSAR; atmospheric correction; topographic correction; modified 3D unwrapping; Damavand volcano; Mosha Fault

1. Introduction

Monitoring of ground deformation due to natural and anthropogenic hazards provides valuable information for various stages involved in disaster cycle response, from pre-disaster risk reduction to mapping the effects of an event for post-disaster management. Remote sensing measurements using techniques such as Interferometric Synthetic Aperture Radar (InSAR) are becoming increasingly important in such studies as they provide regional and spatially-continuous maps of deformation with great accuracy (< cm), without the need of performing much field work or expensive ground surveys [1–6].

InSAR technique uses radio signals propagating through the Earth's atmosphere. The speed and direction of these waves are altered by electrically-neutral and -charged regions of the atmosphere, causing path delay and advance, respectively.

Tropospheric-induced error sources affect the quality of interferometric phase measurements, and reduce signal to noise ratio in the estimation of deformation signal [7–9]. The problem becomes more serious when using short wavelength SAR systems, such as TerraSAR-X and COSMO-SkyMed, which are more sensitive to such error sources [10].

The other limiting factors of InSAR are temporal decorrelation, which causes the loss of coherence due to changes in surface cover, and geometrical decorrelation, which causes the loss of coherence in areas with steep terrain due to variation of the observed angle for each resolution cell during the two acquisitions [11]. All of the limiting factors contribute to the decreasing quality of the interferograms.

Using more than two SAR scenes leads to redundant observations, which can be used to mitigate the effects of decorrelation and atmospheric artifacts in interferometric observation [12–14]. There are three broad categories of multi-temporal methods that deal with decorrelation phenomena in InSAR observations. These are PS-InSAR, SBAS, and SAR tomography techniques. The PS-InSAR relies on the analysis of interferograms with respect to one master image, in which the decorrelation problem is solved through identifying pixels, the so-called permanent/persistent scatterers, their scattering properties have little variations with time and look angle. The permanent scatterers can be used to provide high precision and high density displacement measurements over long periods of time [15–22]. The SBAS algorithm uses all possible SAR image combinations with a small temporal and spatial baseline to reduce spatial decorrelation and the effect of residual phase due to uncompensated topography [23–28]. The SAR tomography uses multiple views to profile the scattering power at different heights [29].

In spite of the many merits of both PS-InSAR and SBAS methods there has been some debate on how to efficiently perform these algorithms on mountainous areas with drastic changes in topography [21,30–33]. In this paper, we present an algorithm to improve SBAS method that has been implemented in the StaMPS [12,34] in order to better estimate slow deformation in the center of the Alborz Mountains, Iran. In our analysis, we used both C-band Envisat and L-band ALOS data. The Envisat SAR data suffer more from high geometric decorrelation in mountainous regions but have high sensitivity to detect slow deformation while ALOS SAR data have lower geometric decorrelation but less sensitivity than Envisat to detect slow deformation. We applied an improved multi-temporal method to both Envisat and ALOS data dealing with several stages in time-series analysis. These are filtering prior to phase unwrapping, topography correction within 3D unwrapping (equipped 3D-unwrapping to topographic correction), and correcting for atmospheric artifacts using GPS data.

This paper is structured as follows. Our Improved SBAS algorithm (here called ISBAS) is described in Section 2. Applicability of ISBAS for Envisat and ALOS data to assess tectonic and volcanic deformation in the Alborz region is described in Section 3. Sections 4 and 5 are dedicated to discussion and conclusions, respectively.

2. Improved SBAS Algorithm

In this paper, we used the SBAS method that has been implemented in the StaMPS [12,34] as the basis for our work. In StaMPS, the specific identification of pixels for the time-series analysis is done based on single-look interferograms that are coherent in time [19]. Another advantage of the StaMPS method is the ability to do 3D phase unwrapping in both spatial and temporal domain to retrieve the absolute phase retrieval of each pixel.

The StaMPS approach either for PS or SBAS method works well for deformation analysis in different applications (e.g., [2,3,5,6,10,35,36]). It starts with the formation of single (for PS) or multiple masters (for SBAS) single-looked interferograms from the available coregistered SAR pairs. The SBAS interferograms are characterized by small temporal and spatial baselines as well as by a small frequency shift between the Doppler centroids. An initial set of coherent pixels is first selected based on amplitude analysis. Then the final selection of pixels is done based on phase stability analysis. In this step pixels must be prepared for the unwrapping process, which is done using the 3D unwrapping method. This method works well only for well-sampled cases in which Nyquist assumption has been satisfied [35,36], under the assumption the unwrapped phase values of neighboring PSs lie within half a cycle. Such conditions may not be easily met in mountainous areas because of existing geometric decorrelation as well as residual topographic errors and atmospheric artifacts. Therefore, the use of the StaMPS in mountainous areas is very challenging. In this study we improved the SBAS method implemented in StaMPS to improve the time series quality using SAR data. Figure 1 shows the diagram of our proposed methodology, which is described in detail below.

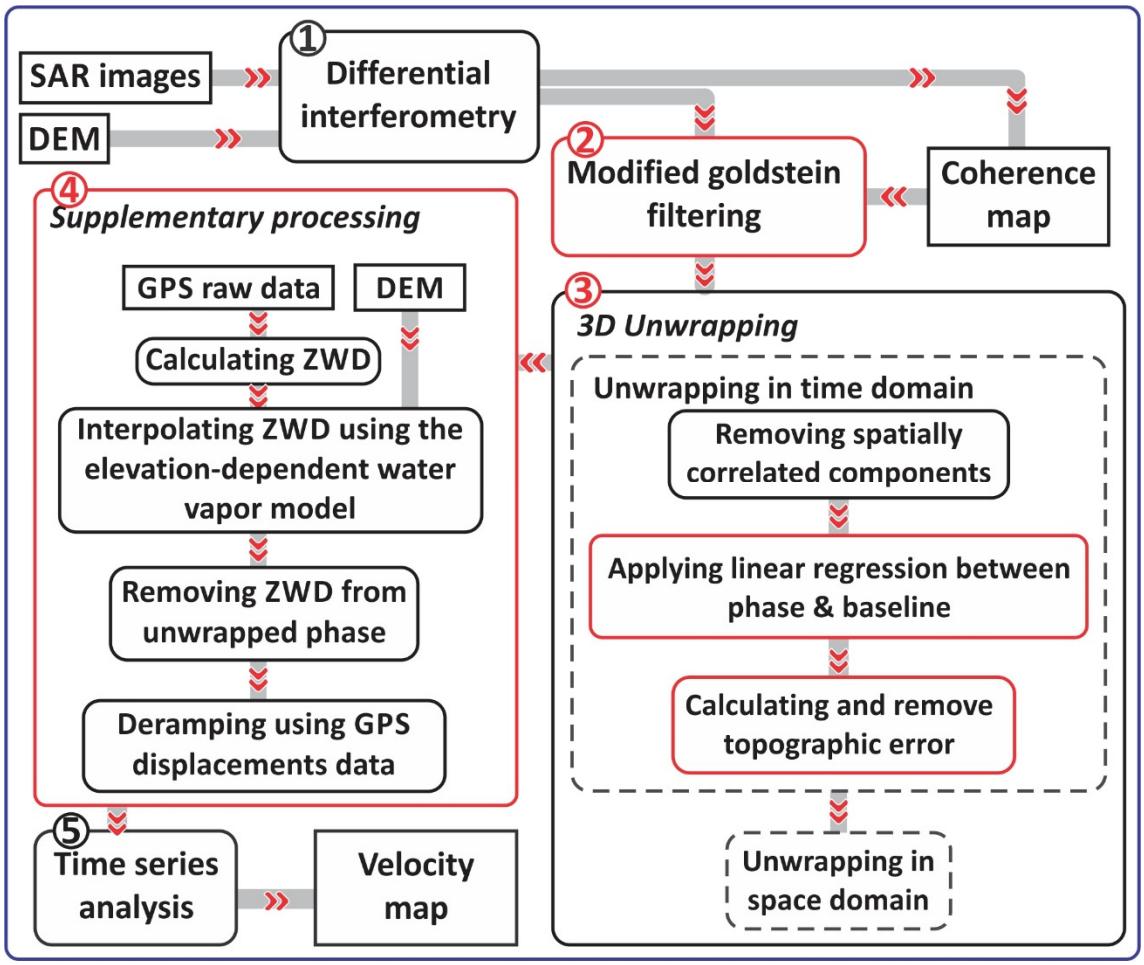

Figure 1. Improved SBAS diagram; the red boxes mark the modified and supplementary processing steps proposed in this study.

2.1. Modified Filtering

The first modification was interferometric phase filtering prior to phase unwrapping. StaMPS uses the standard Goldstein filter [37] to reduce decorrelation noise before phase unwrapping. The Goldstein filter is an adaptive filter that is commonly used to reduce the noise contributions from the interferogram. In performing this filtering, Fourier spectrum of the small patch $Z(u,v)$ is multiplied by its smoothed absolute value $S\{|Z(u,v)|\}$ (1) [37]:

$$H(u,v) = S\{|Z(u,v)|\}^{\propto} \cdot Z(u,v) \quad (1)$$

where α is the filter parameter, Z(u,v) is the Fourier transform of a small interferogram patch; H(u,v) is the filter response; S{} is a smoothing operator and u and v are spatial frequencies.

In the standard Goldstein method, the filter parameter α is kept constant over the entire processed area. This is not efficient for mountain areas with many decorrelated regions. Baran *et al.* (2003) presented a modified Goldstein filter in which the filter parameter is selected based on coherence value [38].

$$H(u,v) = S\{|Z(u,v)|\}^{1-\overline{\gamma}} \cdot Z(u,v) \quad (2)$$

where γ is the coherence value. This modification allows stronger filtering on incoherent areas. We further modified the filtering parameter α using the following logarithmic equation to increase the efficiency of filtering especially for incoherent areas:

$$H(u,v) = S\{|Z(u,v)|\}^{\overline{\log(1-\gamma^3)}} \cdot Z(u,v) \quad (3)$$

As will be discussed in Section 4, this modification allows stronger filtering of the incoherent area, improving the quality of the unwrapped results.

2.2. Improving the Interferometric Phase Unwrapping

Following the topographic and geometric correction in repeat-pass interferometry, the remaining phase shift in interferometric observation can be expressed as a function of several components including deformation, the difference in atmospheric retardation between passes, orbit inaccuracies, and residual topographic error in the DEM. StaMPS assumes that the first three phase components are spatially correlated over a specific distance and, therefore, mitigate their effects by subtracting the average of the phase of all those pixels within a circular patch centered on each permanent pixel from the measured interferometric phase [12].

For the residual topographic error ($\phi\varepsilon$), which is uncorrelated over the same distance, the relationship between this component and perpendicular baselines is linear and is described as:

$$\phi_\varepsilon(t_i,t_j) = \frac{4\pi}{\lambda}\frac{B_\perp(t_i,t_j)}{rsin(\theta)}(Z^e), K_\varepsilon = \frac{4\pi}{\lambda}\frac{Z^e}{rsin(\theta)} \quad (4)$$

where $B_\perp(t_i,t_j)$ is the perpendicular baseline between the two time acquisitions (t_i and t_j), r is the SAR range between SAR sensor and target, θ is the look angle and Z^e is the DEM error. StaMPS estimates the proportionality constant ($K\varepsilon$), which is the ratio between $\phi\varepsilon$ and baseline for each permanent pixel in a least square sense before performing the 3D unwrapping process. Then irregularly sampled pixels in time are unwrapped using 3D unwrapping algorithms [35], which unwraps pixels in both time and space domain separately. For the unwrapping in time, the algorithm defines edges connecting data points using Delaunay triangulation and then calculates edge phase differences between the differential (interferometric) phases of neighboring pixels. In this way, only spatially correlated effects including atmospheric and orbital errors are removed but there remains several undersampled areas that have to be corrected. The existence of any spatially correlated or uncorrelated components which can happen (e.g., in mountainous areas due to DEM error and noise due to geometric decorrelation) makes the difference between sequential values more than half a cycle, in turn disturbing the unwrapping process in time.

StaMPS solution for adjusting these areas (time undersarmpled areas probably caused by DEM error), for either the PS or SBAS method is to apply the averaging filter in time domain, regardless of the source of error. However, in our implementation we assume that the existing undersampled areas are related to uncertainty in estimation of $K\varepsilon$ due to strong correlation between the differential phase of neighboring pixels ($\delta\phi^e_{topo}$) and baselines. This correlation is significant in particular for processing of ALOS dataset with large spatial baseline. To estimate residual topographic ratio, we therefore apply linear regression between the calculated term $\delta\phi^e_{topo}$ (measured edge phase differences) and $B_\perp$. This makes the phase difference in time (*i.e.*, the phase difference of each acquisition inverted from the resulted phase values of all SBAS pairs) smoother. The resulted phase difference time series is temporally filtered by low-pass filter in frequency domain using a Goldstein window. This averaging operator helps also mitigate contribution from any unaccounted components including thermal noise. The filtered phase

difference is inverted using weighted least square to retrieve the phase of each pixel. We use the inverse of the standard deviation for the difference between the edge time series as the weighting factor. Spatial unwrapping is finally performed after interpolating coherent pixels of interferograms in regularly gridded data using nearest neighbor method. In this step absolute topographic errors are first computed from edge difference wrapped phases, and then are subtracted from the unwrapped interferograms to compensate for residual topographic errors. Figure 2 shows an example of ALOS interferogram, which was unwrapped with standard technique and with our modified unwrapping method. Clear improvements in the results are recognizable in Figure 2 in which most of the disturbances related to topographic errors are removed after correction (Figure 2b).

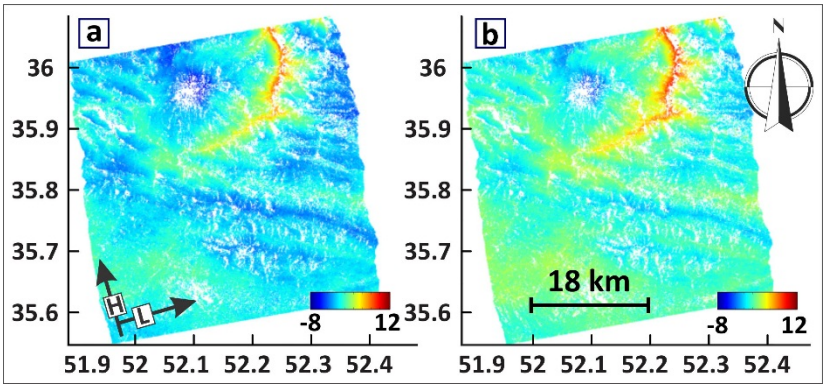

Figure 2. Comparison of unwrapped interferograms for ALOS interferometric pairs of 24 July 2007 and 13 June 2009 produced by (**a**) StaMPS and (**b**) our modified unwrapping method. The perpendicular baseline is 1290 m.

2.3. Supplementary Processing

After modifying the phase unwrapping process in the time-series analysis, atmospheric correction needs to be implemented on each interferogram separately. This step is performed after the unwrapping process [39]. However there are some studies in which the correction for atmospheric artifact is done before unwrapping in order to reduce the risk of phase unwrapping errors in regions of rough topography [10,28], especially when the coherence of interferometric pairs is low [40]. In this paper, we used atmospheric correction after the 3D unwrapping process. Using 3D unwrapping with the ability of separating spatially correlated components on one hand and relatively fair coherence of the interferometric pairs on the other hand, makes it possible to mitigate phase unwrapping errors considerably.

In this work, we used GPS data to model troposphere effect based on an elevation-dependent interpolator (Figure 3). There are three elevation-dependent water vapor interpolations including the Best Linear Unbiased Estimator in combination with the water vapor Height Scaling Model (BLUE + HSM) [41], the Best Linear Unbiased Estimator coupled with the Elevation-dependent Covariance Model (BLUE + ECM) [42], and the Simple Kriging with varying local means based on the Baby semi-empirical model (SKlm + Baby) [43]. In this study we used the revised version of the SKlm + Baby model that is presented by Xu *et al.* [44] to model the elevation-dependent component of the water vapor delay. In this model the more straightforward elevation-related regression function (Onn water vapor model) replaces the inaccurate Baby semi empirical model [45].

We processed GPS data using Point Positioning (PPP) technique [46] in the GIPSY software to estimate Zenith Wet Delay (ZWD) parameter. We derived ZWD from the data collected by five GPS stations [47] (depicted by black squares in Figure 4) and interpolate them using the elevation-dependent water vapor model [7].

$$Z^*_{SKlm}(u) = \sum_{i=1}^{n} \omega_i^{SK}[Z(u_i) - m^*_{SK}(u_i)] + m^*_{SK} \tag{5}$$

where $Z^*_{SKlm}(u)$ denotes the interpolated water vapor delay at location u; $Z(u_i)$ represents the measured water vapor delay at location u_i; n is the number of measured water vapor delays used for the interpolation; w_i^{SK} are the Kriging weights to be determined; m^*_{SK} denotes the elevation-dependent component of water vapor delay at locations u and is estimated from the Onn water vapor model by Equation (6):

$$m^*_{SK} = Ce^{-\propto h} + h \propto Ce^{-\propto h} + Z_{min} \tag{6}$$

where C is proportional to the amount of ZWD measured at sea level, α is the delay rate of the vertical water vapor profile, and Z_{min} is the ZWD value at the highest location. C, α and Z_{min} can be estimated by regression analysis.

After applying the related tropospheric correction, the remaining errors due to ionospheric turbulence or orbital errors are removed by fitting a ramp to the data. For those dates that we had operating local GPS stations in our study area, the ramp is removed by fitting a plane to GPS displacements. For other dates the ramp removal processing is performed by least squared analysis in the same way as the standard processing tools [48].

Figure 3 shows an example of atmospheric and orbit/ionospheric correction for interferometric pair of 24 July 2007 and 13 September 2009. As seen in Figure 3, the correlation between corrected interferometric phase and DEM which is due to temporal changes in atmospheric stratification is reduced by 80% after applying the related corrections. The confidence level for the correlation coefficients was determined at the 95% significance level.

Although the differential phase between neighboring permanent pixels after removing topographic effect is small and their effects on unwrapping are negligible, their cumulative effects over larger areas at the end of 3D unwrapping are significant. Therefore, in this study an additional residual DEM correction was performed after atmospheric and orbital corrections to remove the remaining DEM errors. To that end, we formed the following system of equations to estimate residual topographic components from the measured phase:

$$\begin{bmatrix} \Delta T1 & B_1 \\ \Delta T2 & B_2 \\ \vdots & \vdots \\ \Delta Tn & B_n \end{bmatrix} \begin{bmatrix} 1 & 0 & 0 & \dots & 0 \\ 1 & 0 & 0 & \cdots & 0 \\ 0 & 1 & 0 & \cdots & 0 \\ 0 & 1 & 0 & \cdots & 0 \\ \vdots & \vdots & \vdots & \vdots & \vdots \end{bmatrix} \begin{bmatrix} V \\ K \\ \phi_1^M \\ \phi_2^M \\ \vdots \\ \phi_i^M \end{bmatrix} = \begin{bmatrix} \Delta\phi_1 \\ \Delta\phi_2 \\ \vdots \\ \Delta\phi_n \end{bmatrix} \tag{7}$$

where ΔT_i and B_i are time interval and perpendicular baseline of i^{th} pairs, respectively, V is the velocity, K is proportionality constant (K) between phase and baseline, ϕ_i^M is the spatially correlated component of the i^{th} master images. The column with perpendicular baselines has been added to design matrix A in order to compensate for the effect of residual DEM error. We have estimated unknown parameters by

applying SVD to matrix A to obtain the least squares solution for the linear component of the displacement, topographic correction, and atmospheric component.

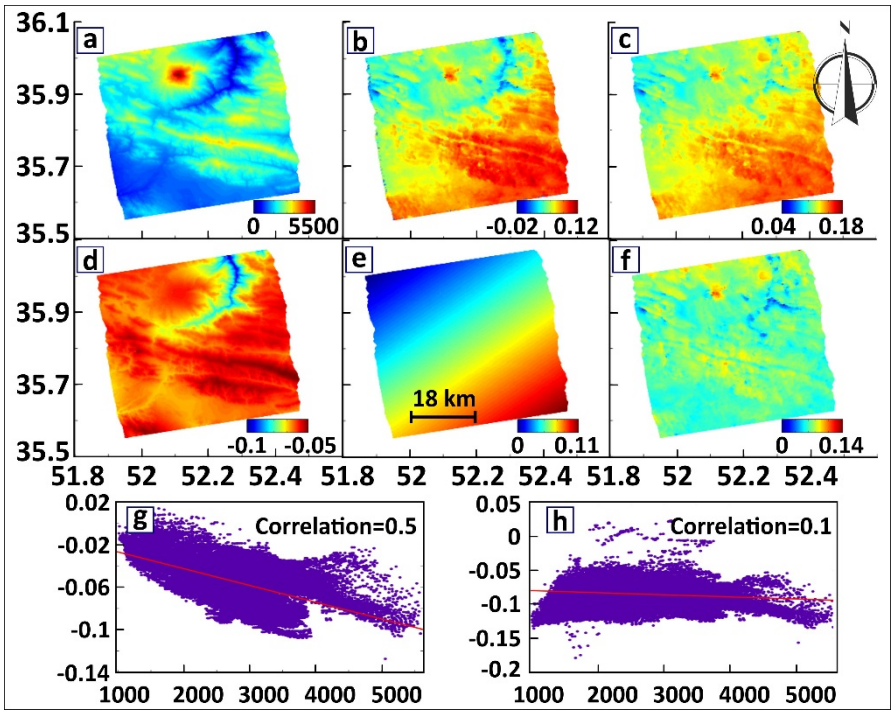

Figure 3. Atmospheric and orbits/ionosphere correction for ALOS interferometric pair of 24 July 2007 and 13 September 2009. (**a**) SRTM DEM, elevation in meters; (**b**) Original interferogram. (**c**) Differenced wet delay map along LOS direction derived from GPS data and elevation-dependent interpolator; (**d**) Corrected interferogram after removing tropospheric effects; (**e**) Estimated orbit/ionospheric ramp; (**f**) Corrected interferogram after removing orbits/ionosphere effects. Note that negative values imply the ground surface moves away from the satellite and positive values move toward the satellite (colorbar in meter). (**g**) and (**h**) illustrate correlation between interferometric phase (original and corrected) and SRTM Digital Elevation Model, corresponding to (b) and (f) respectively.

3. Experimental Study

In order to assess the performance of our improved method, we used all SAR data acquired by the Envisat satellite during 2003–2009 and ALOS satellite during 2007–2009 to monitor surface deformation in the center of the Alborz Mountains, north-east of Tehran (Figure 4). We selected this region because of existing potential geodynamic targets in the area, including possible volcanic deformation associated with the Damavand volcano and interseismic deformation associated with the Mosha fault, active structures in southern tip of Central Alborz.

Figure 4 illustrates a shaded relief map of the study area, the location of the continuous GPS (CGPS) and survey mode GPS (SGPS) sites and the coverage of SAR data used in this study. The networks of small baseline interferograms that were used for time-series analysis are presented in Figure 5. A total number of 69 and 47 Envisat interferograms were processed using descending and ascending images, respectively. Moreover, 12 ascending interferograms were processed using ALOS data.

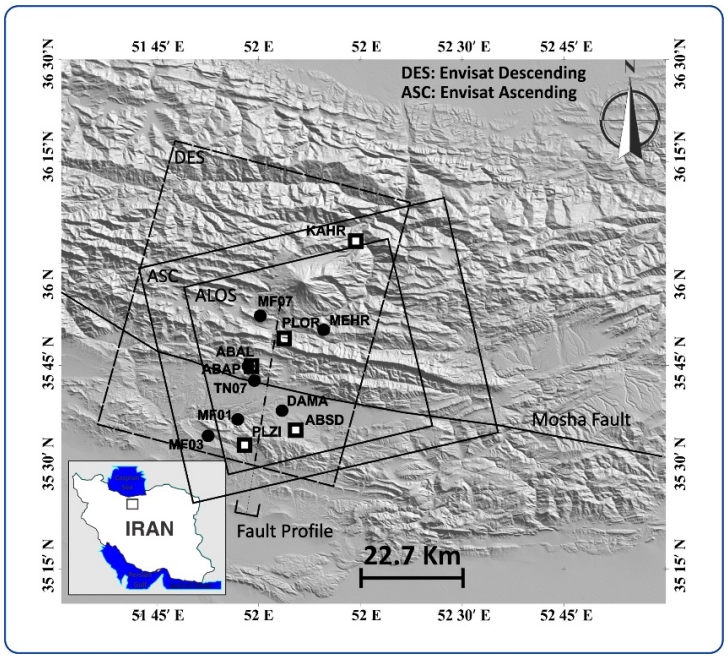

Figure 4. Shaded relief map of the study area. Black boxes represent SAR coverage from ALOS, Ascending Envisat (ASC) and Descending Envisat (DES). The inset map shows location of the study area in Iran. The Location of CGPS and SGPS located in the study area are depicted by square and circle, respectively. The dashed line shows the location of the profile used for Mosha fault analysis.

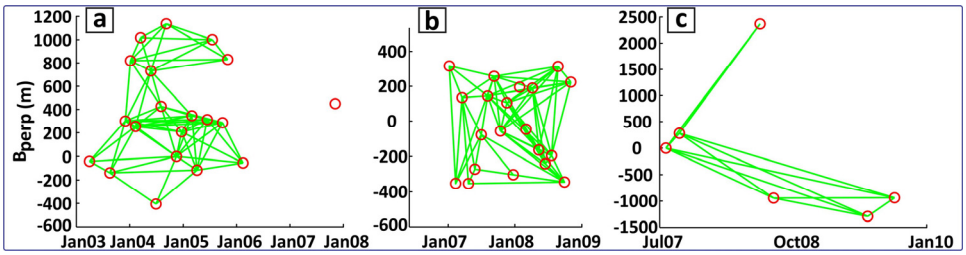

Figure 5. The network of small baseline interferograms for (**a**) Envisat ascending (**b**) Envisat descending and (**c**) ALOS ascending orbits.

StaMPS Processing vs. ISBAS Processing

Figure 6 shows the resulted velocity map that we obtained using the standard method implemented in StaMPS and by our ISBAS method in this paper for the Envisat descending (Figure 6a,d), Envisat ascending (Figure 6b,e) and ALOS data (Figure 6c,f). The InSAR velocity results in Figure 6 are with respect to the reference point (black circle), selected near the GPS station PLOR that is located outside the Damavand area.

This figure clearly shows that the ISBAS has been able to overcome a lot of short wavelength and long-wavelength artifacts that are clearly visible in StaMPS results. For example, the influence of artifacts resulted from topography-dependent atmospheric turbulence seen in the Figure 6a–c have been greatly reduced in Figure 6d–f, allowing us to better analyze ground deformation in this area. Interestingly, the standard processing shows significant LOS subsidence around the Damavand volcano

for the Envisat descending and ALOS, which is not seen in the ISBAS results. In the following section, we analyze in detail the difference between ISBAS and StaMPS (Figure 6) for the Damavand volcano and Mosha fault and address the implications that the results have for understanding of geophysical processes at these two targets.

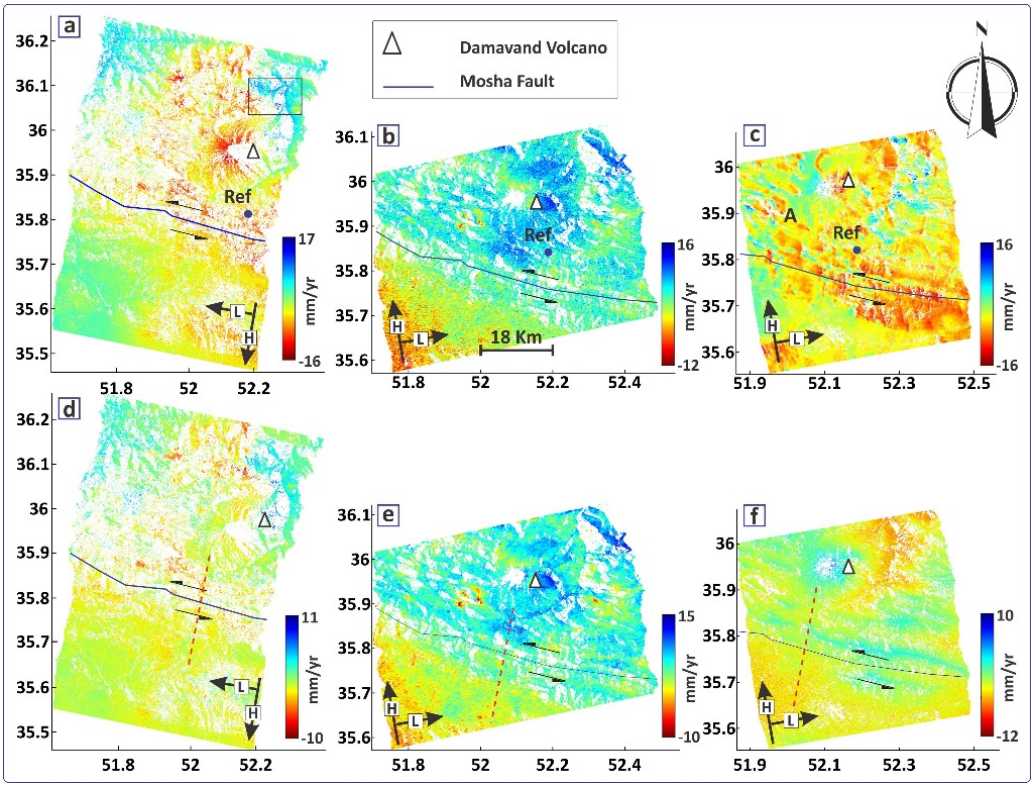

Figure 6. Deformation velocity map obtained from StaMPS for (**a**) Envisat descending (**b**) Envisat ascending and (**c**) ALOS. The location of the Damavand volcano is depicted by a black triangle. (**d**), (**e**) and (**f**) represent the ISBAS final results from Envisat descending, Envisat ascending and ALOS ascending dataset, respectively. Thick black arrows illustrate directions of the satellite track (H) and LOS vector (L). The Mosha fault is indicated by a dashed black line. The reference point, near PLOR station, is depicted by a black circle in (a), (b) and (c).

Damavand Volcano

In Figures 7–9 we analyze the relation between topography and LOS displacement from both StaMPS and ISBAS results for an arbitrary NE-SW profile in Damavand.

For the Envisat descending data (Figure 7), the StaMPS provides a correlation coefficient of −0.8 while this value in the ISBAS method reduces to only −0.4. The same improvement can be seen in Envisat ascending (Figure 8; −0.5 in StaMPS *vs.* −0.2 in ISBAS) and in ALOS data (Figure 9; −0.8 in StaMPS *vs.* −0.4 in ISBAS). This reduction in correlation coefficients shows that the ISBAS method has worked better than StaMPS in mitigating the effect of topography-dependent atmospheric turbulence on the time-series results.

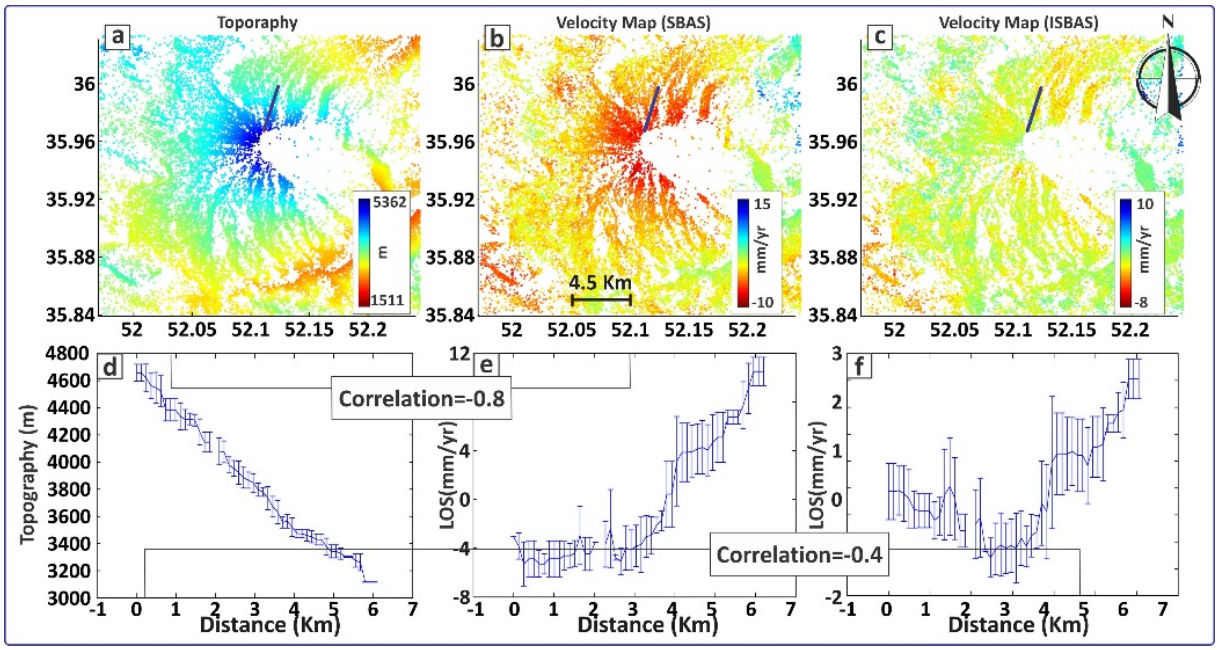

Figure 7. (**a**) Topographic map. (**b**), (**c**) are ground deformation velocity maps from Envisat descending data calculated by standard SBAS and ISBAS methods, respectively. (**d**) Topographic profile extracted from (a). (**e**) and (**f**) are displacement profiles extracted from (b) and (c), respectively. Correlation coefficients were determined at the 95% confidence level.

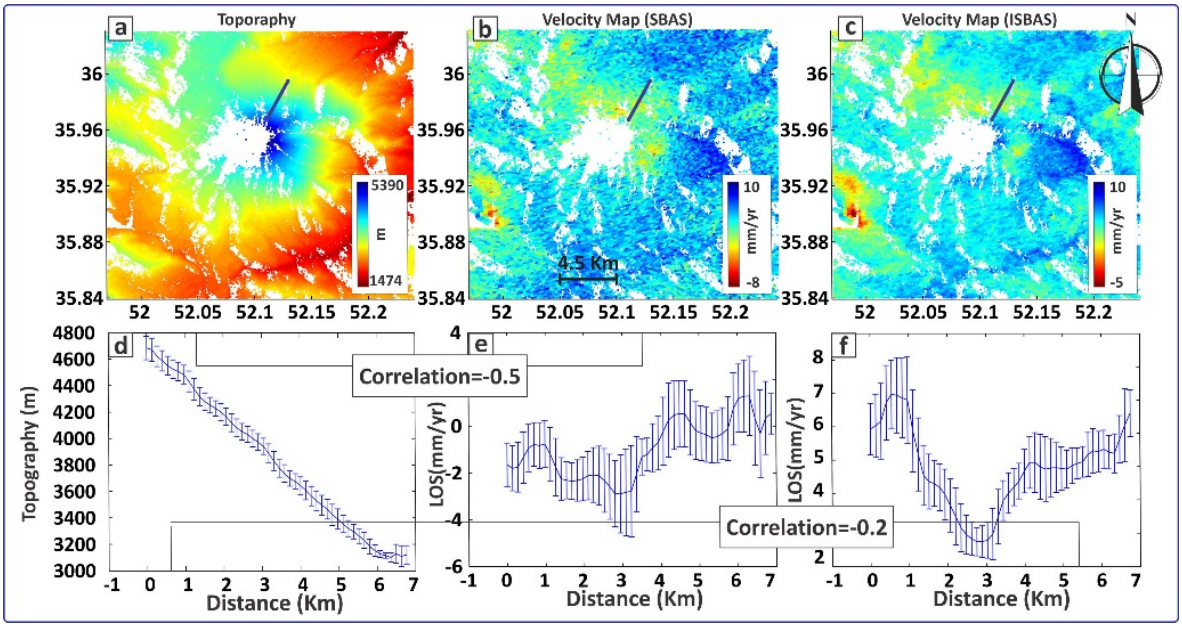

Figure 8. (**a**) Topographic map. (**b**), (**c**) are ground deformation velocity maps from Envisat ascending dataset calculated by standard SBAS and ISBAS methods, respectively. (**d**) Topographic profile extracted from (a). (**e**) and (**f**) are displacement profile extracted from (b) and (c), respectively. Correlation coefficients were determined at the 95% significance level.

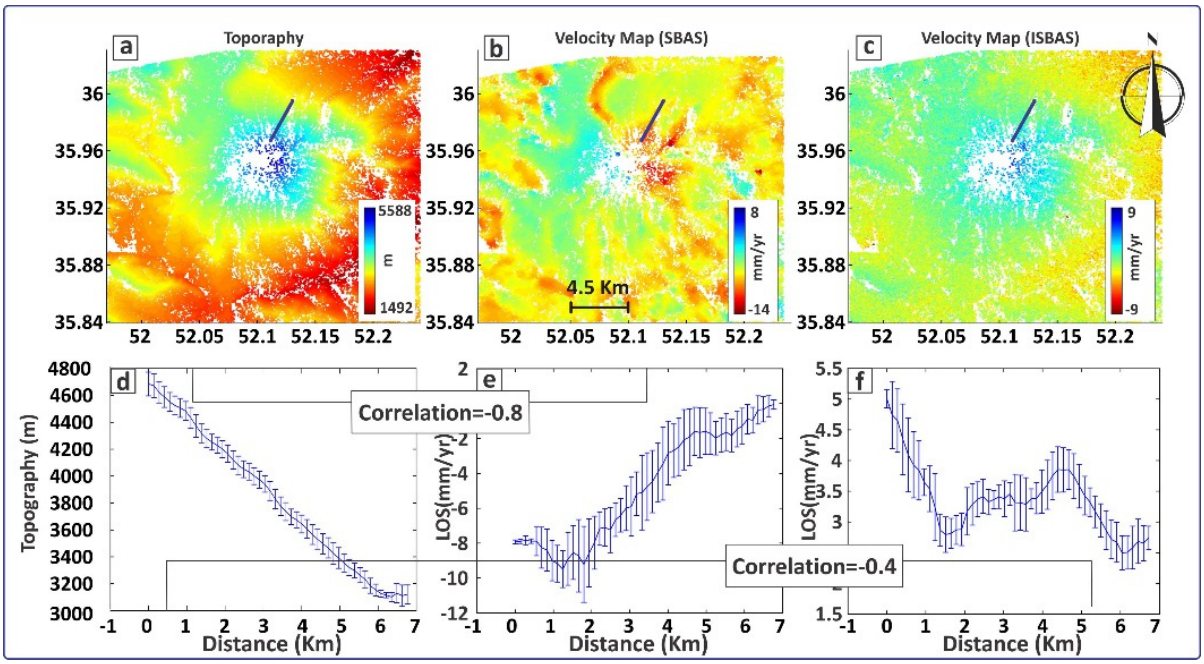

Figure 9. (**a**) Topographic map. (**b**), (**c**) are ground deformation velocity maps from ALOS dataset calculated by standard SBAS and ISBAS methods, respectively. (**d**) Topographic profile extracted from (a). (**e**) and (**f**) are displacement profile extracted from (b) and (c), respectively. Correlation coefficients were determined at a 95% confidence level.

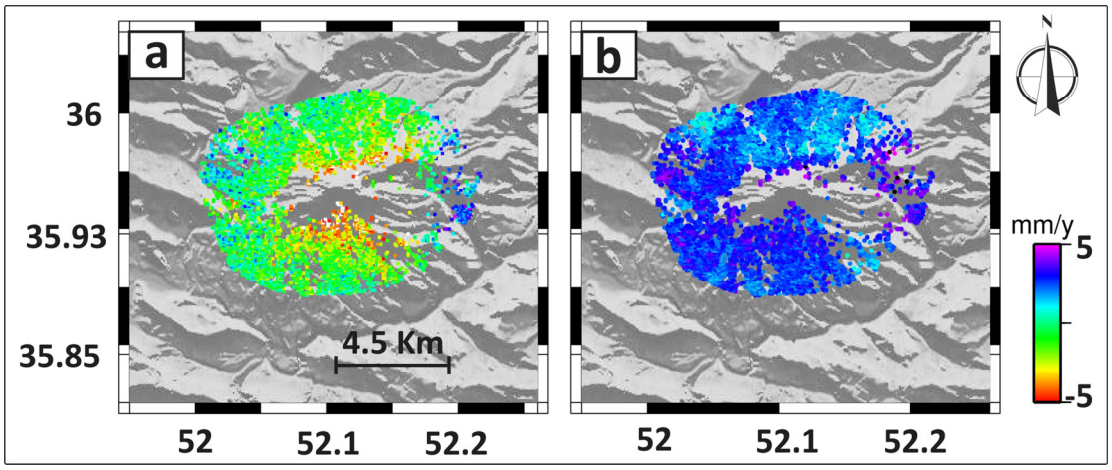

Figure 10. Decomposition of LOS displacement to vertical and horizontal components. (**a**) East-west motion; negative values correspond to motion toward the west and positive values towards the east. (**b**) Vertical motion; positive values correspond to uplift.

In this study as three InSAR measurements from ascending and descending geometries are available for Damavand, the LOS results are decomposed to retrieve 2D maps of east-west and vertical displacement [49]. Figure 10 shows the decomposition of LOS displacement to horizontal and vertical components around the Damavand volcano. We ignored the north-south component because of lowest sensitivity of InSAR observations to the north-south component.

As shown in Figure 10b, the vertical velocity around Damavand retrieved from InSAR observations shows a broad uplift on the order of 3 mm/year (The mean for all pixels around Damavand). The

decomposition also reveals an overall westward displacement on the northern and southern slopes (Figure 10a).

Mosha Fault

Figures 11–13 show topography and fault-parallel velocity along a 50 km profile perpendicular to the surface trace of the Mosha Fault, corresponding to Envisat descending, Envisat ascending and ALOS dataset, respectively. We also processed GPS measurements of 9–11 stations, including SGPS (survey mode GPS) from 2000 to 2008 and CGPS (continuous GPS) sites installed since 2005 (Figure 4) [50], to estimate fault parallel velocities.

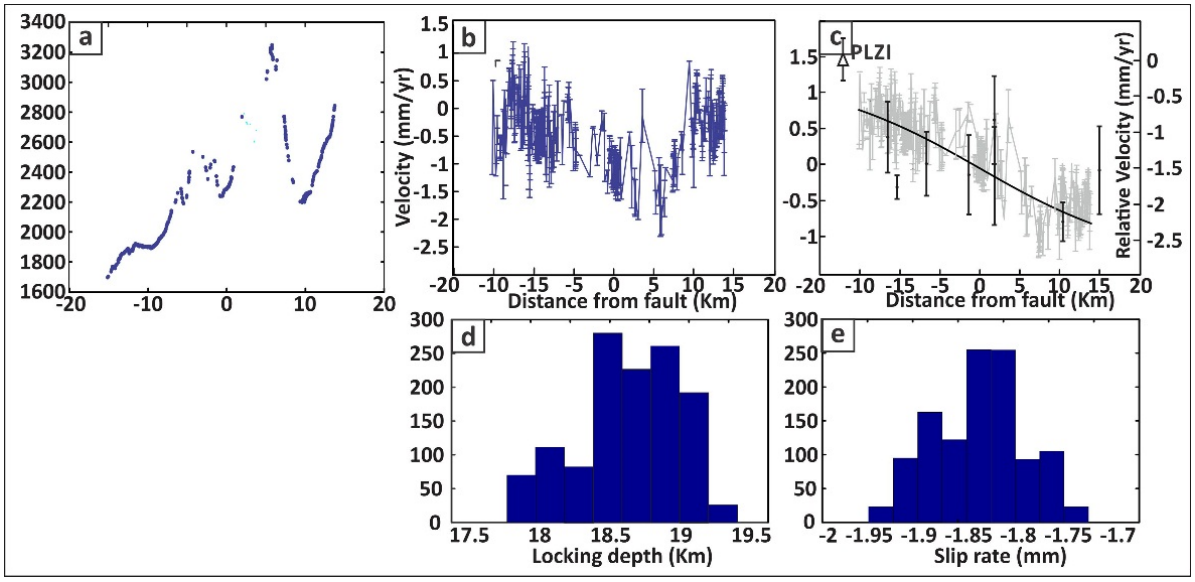

Figure 11. Fault parallel velocity profile spanning 2003–2006, along a profile shown by red dashed line in Figure 6d–f. (**a**) Topographic profile. (**b**) Stamps velocity. (**c**) ISBAS velocity and fit to deformation data using elastic half-space model. The black line shows the best fit model. The black dots are velocities obtained from GPS observations. The axis of relative velocity corresponds to fault-parallel velocity estimated from GPS observations with respect to the station PLZI (marked by black rectangle). Probability distribution for the (**d**) locking depth and (**e**) slip rate determined from the bootstrap method. InSAR-derived velocity values are relative to the profile center.

For Envisat observations, the average discrepancy between GPS and InSAR results is about 0.88 mm/year before applying ISBAS and is decreased to 0.42 mm/year after ISBAS processing. For the ALOS measurements the estimated difference is about 1.2 mm/year before applying ISBAS and is decreases to 0.66 mm/year after ISBAS processing. Therefore, we found an improvement of about 52% and 44% on the accuracy of the calculated velocity for Envisat and ALOS dataset, respectively.

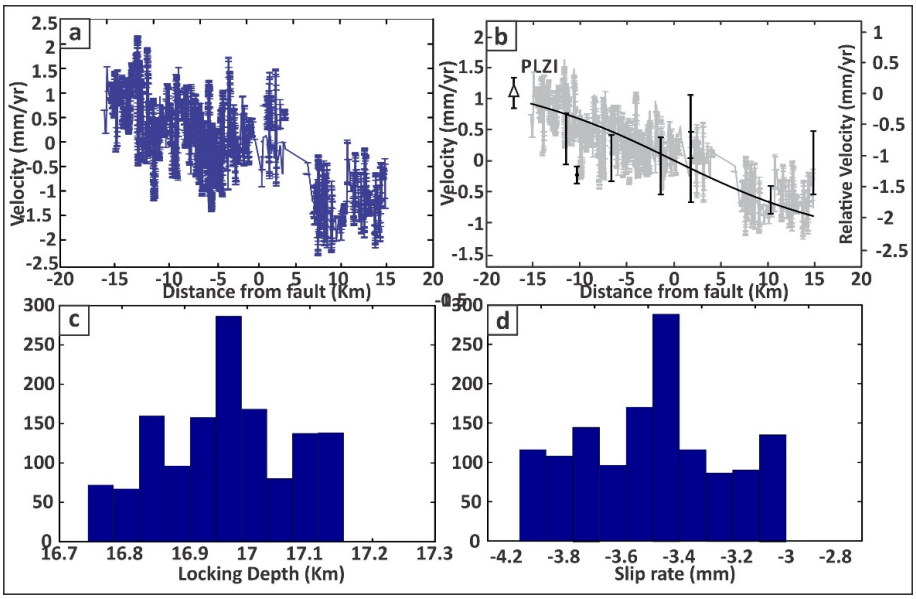

Figure 12. 2007–2009 fault-parallel velocity profile derived from Envisat ascending data using (**a**) StaMPS and (**b**) ISBAS methods. Probability distributions for the (**c**) locking depth and (**d**) slip rate from bootstrap analysis of ISBAS results.

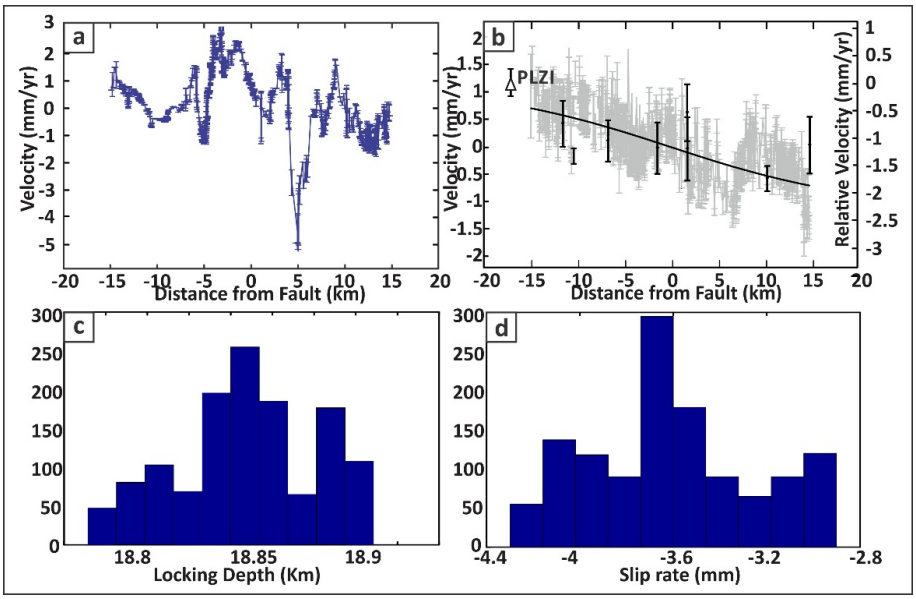

Figure 13. 2007–2010 fault-parallel velocity profile derived from ALOS data using (**a**) StaMPS and (**b**) ISBAS method. Probability distribution for the (**c**) locking depth and (**d**) slip rate.

As seen in Figures 11–13, the modification performed in the ISBAS is able to provide a better picture for interseismic strain accumulation around the Mosha fault. We used these observations to estimate the parameters of the first-order interseismic model, in which aseismic left-lateral strike-slip(s) occurs on a vertical plane beneath a locked crust of thickness H [22]. In this model the fault-parallel velocity is given by [51]:

$$v(x) = (s/\pi)tan^{-1}(\frac{y}{H}) \quad (8)$$

where y is the distance normal to the fault, s is displacement rate on the fault below depth H. we assume *a priori* range of 0–30 for both parameters which is large enough to enable reliable estimation. Then we find the best values that minimize the misfit between the calculated profile by the model and the observed profile by InSAR observation using the genetic algorithm [52].

Figures 11d,e, 12c,d and 13c,d show the result of 300 models from bootstrap analysis [53] of velocity results in Figures 11c, 12b and 13b, respectively. Both parameters (*i.e.*, slip and depth) in the elastic model are resolved well within *a priori* ranges in the inversion. Our modeling suggests a fault slip rate of ~2–4 mm/year and a locking depth of 17–19 km best matches to the observations.

Comparison with GPS Observations

In this section we compare the results of InSAR time-series from both StaMPS and ISBAS with GPS measurements and show how individual improvements that we performed in atmospheric, orbit, and topographic correction steps increase the quality of the results. Figures 14 and 15 illustrate comparison between Envisat observations and GPS measurements, projected on line of sight for PLZI, ABSD, ABAL and PLOR stations. Figure 16 corresponds to ALOS observations. Original Envisat results obtained from StaMPS show a large discrepancy with GPS measurements at all stations, in particular for dates before 11 May 2008; the smaller discrepancy after 11 May 2008 in Envisat results might be related to the availability of more interferometric pairs after this date (Figure 5b), resulting in better stacking of signal during time-series analysis. As seen in Figures 14–16, by applying atmospheric and orbital corrections, the quality of the InSAR time series results for both Envisat and ALOS are improved by about 70% and 57%, respectively. Applying all the corrections discussed in this paper (ISBAS) further improves the accuracy by 80% and 90% (with respect to standard SBAS processing) for Envisat and ALOS dataset, respectively.

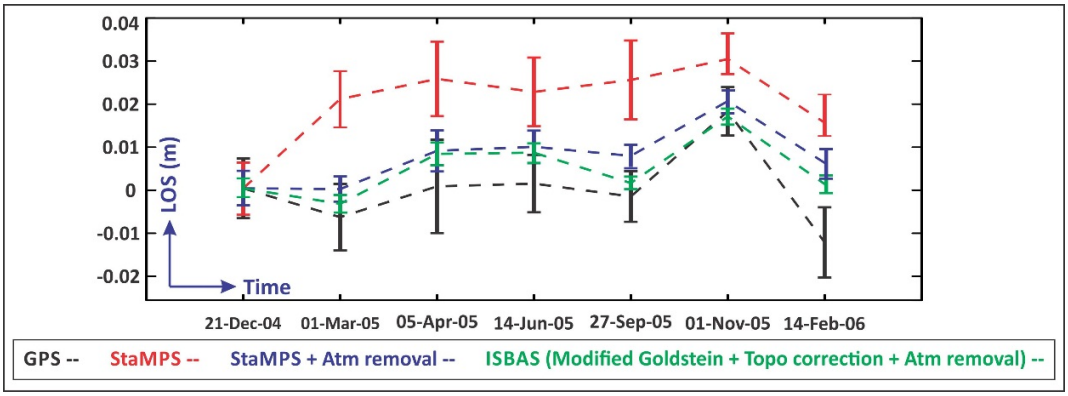

Figure 14. Comparison between GPS-derived LOS displacements and Envisat descending observations for PLOR station.

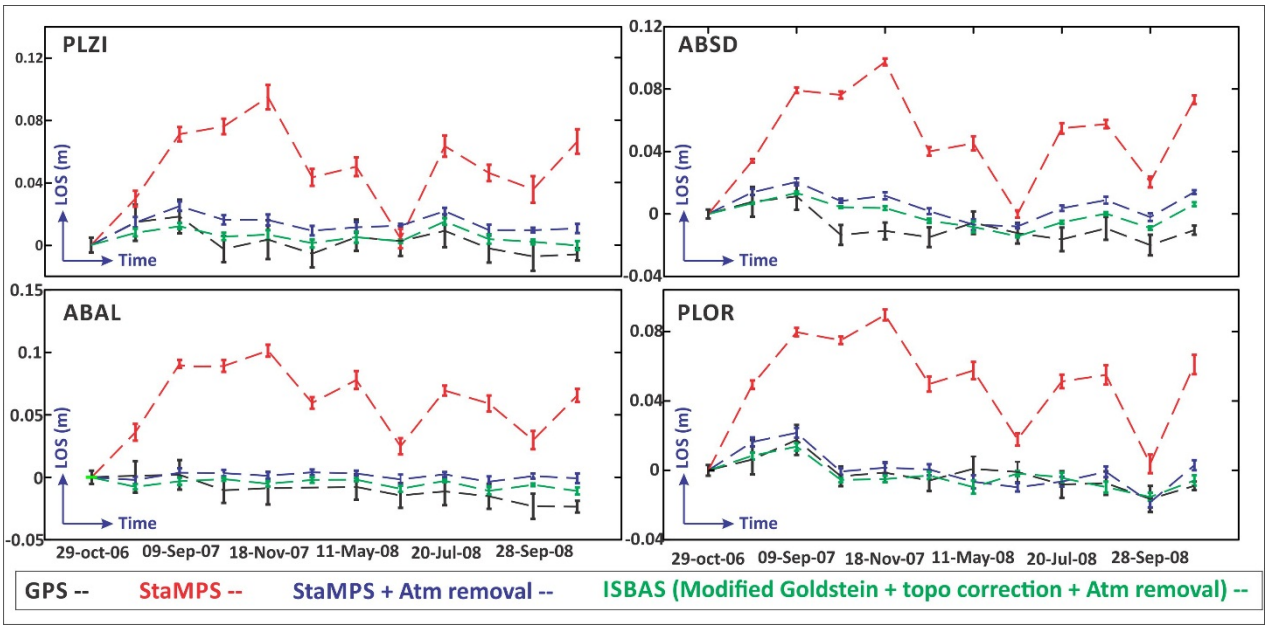

Figure 15. Comparison between GPS-derived LOS measurements and Envisat ascending observations for four GPS stations.

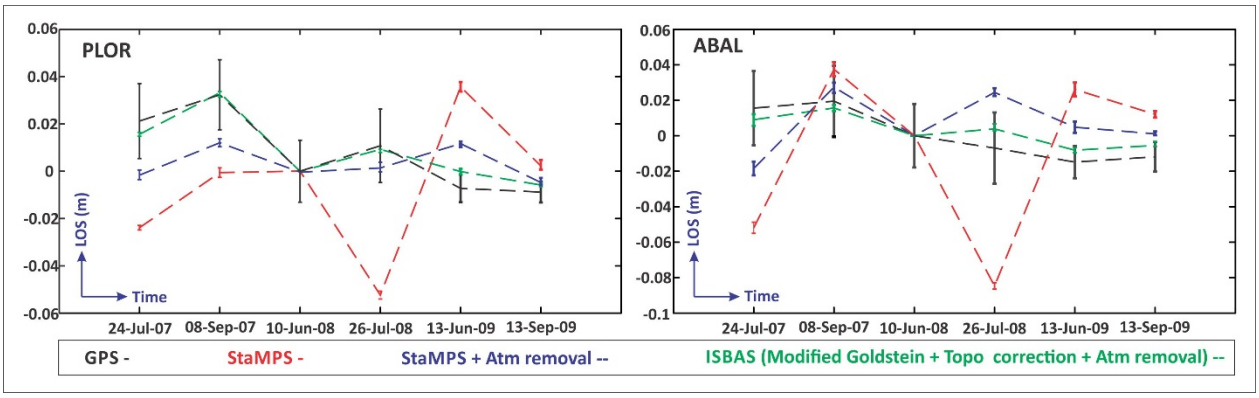

Figure 16. Comparison between GPS-derived LOS displacements and ALOS observations, for PLOR and ABAL stations.

4. Discussion

In this study, we have modified several aspects within the chain of the InSAR time-series analysis in order to improve the quality of the results. The first modification was related to phase filtering in order to make the wrapped phase image as smooth as possible. To achieve this we modified the standard Goldstein filter used by StaMPS and selected the filter parameter (α) based on logarithmic function of coherence value. As shown in Figure 17, such modification allows for a stronger filtering (α value higher than 0.9) in areas with coherence values lower than 0.7, after which the intensity of filtering decreases. This improves the quality of interferograms in areas with low coherence, especially in Envisat interferograms which are affected more by decorrelation noise. This has been illustrated in Figure 18 where we plot global RMS misclosure errors (*i.e.*, mainly unwrapping errors) for all SABS interferograms.

Comparison between the blue, red, yellow bars in the Figure 18a–c, shows the performance of the modified filtering, especially for the C-band dataset which has lower coherence compared with the

L-band dataset. As seen in this figure, applying the modified Goldstein filter reduces unwrapping errors by 60% and 42% for Envisat and ALOS datasets, respectively.

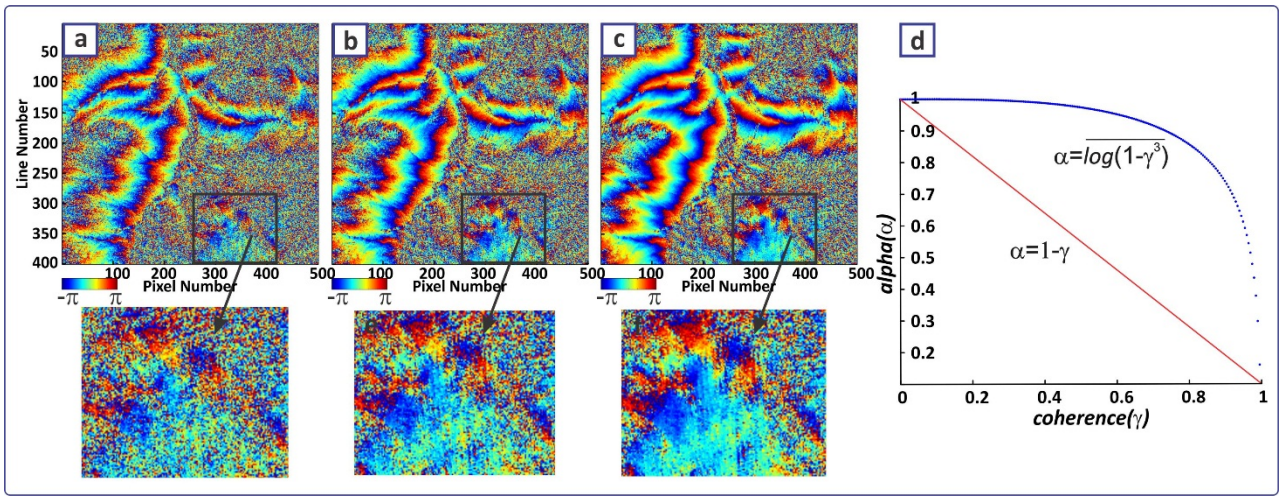

Figure 17. Comparison between standard (used in StaMPS method) and Modified Goldstein filter for a close-up view of the black rectangle in Figure 6. (**a**) Filtered wrapped phase interferogram for standard Goldstein with α ~0.6; (**b**) Modified Goldstein filter from [38] with $\alpha = 1 - \gamma$ (γ: coherence); (**c**) Our modified Goldstein filter with $\alpha = \overline{\log(1-\gamma^3)}$; (**d**) Variation of the α parameter with respect to coherence (γ) value. The red refers to modified Goldstein filtering in [38] while blue refers to our modified filtering.

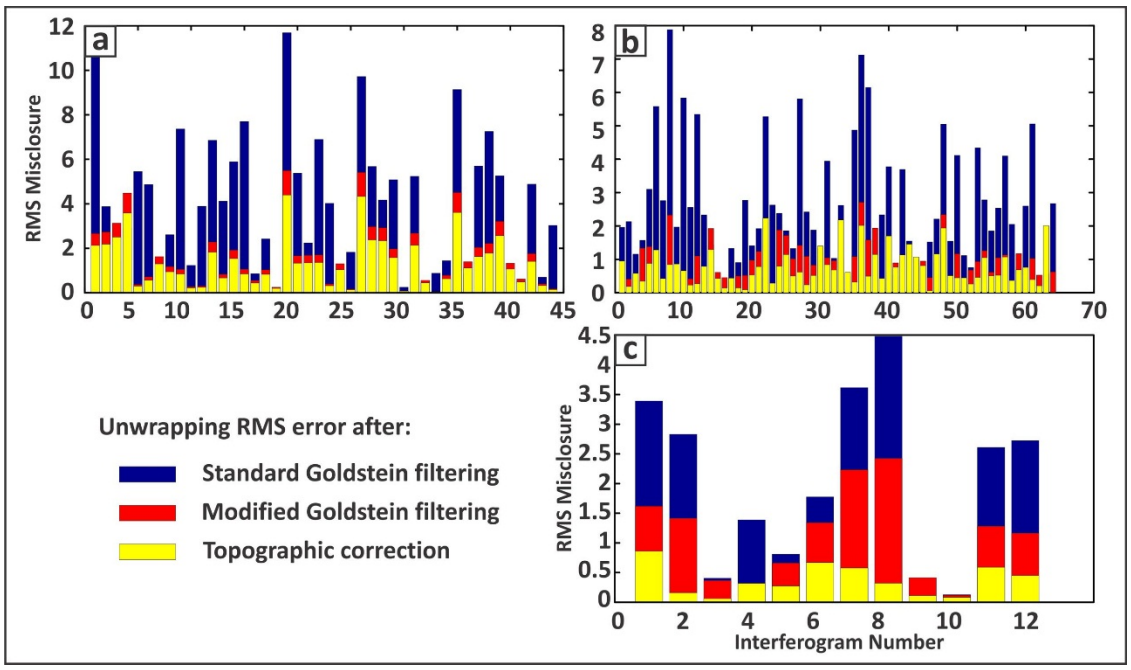

Figure 18. RMS misclosure of each interferogram for the all datasets. (**a**), (**b**) and (**c**) correspond to Envisat descending, ascending, and ALOS dataset respectively. Blue corresponds to the standard Goldstein filter (implemented in StaMPS), red to our modified filtering, and yellow to topographic correction using linear regression.

The second modification is related to performing residual topographic correction within the 3D unwrapping process which is in contrast to the existing topographic correction method in which the DEM error is estimated before/after phase unwrapping [30–32,54,55].

In this regards, we tried to identify noisy pixels (associated with residual topographic noise) either before or after the unwrapping process. The challenging issue here was to detect noisy pixels showing high correlation between phase and baseline. Despite applying an averaging filter over a specific distance, some spatially correlated components always remain which dominate the residual topographic error, in turn causing the estimated correlation map not to show the desired result. For this reason, we performed a linear regression between the measured edge phase difference and perpendicular baselines components within unwrapping in the time domain to better estimate spatial uncorrelated components associated with residual topography errors.

The mentioned correction could also mitigate spatially uncorrelated noise which impeded previous work [35], in which the spatially uncorrelated noise is reduced by low pass filtering. Classical 3D unwrapping works in both time and space domain. In time domain, it reduces first the noise effect by applying a low pass filter on the phase difference in time between neighboring pixels prior to unwrapping in space. However, in our method, the smoothing is done first by evaluating the contribution to noise caused by residual topographic error and removing its effect from time series of differential phase between neighboring pixels. Figure 19 illustrates an example of the phase difference map for the pair which peaks on the global RMS misclosure plot in Figure 18c. As can be seen in Figure 19b, the time-series of differential phase between neighboring pixels is smoother after this correction, which in turn facilitates the performance of 2D spatial unwrapping.

Our experience using Envisat and ALOS data showed that due to the high sensitivity of the L-band sensors to topographic errors and because of their large perpendicular baselines, this correction affects ALOS results more than Envisat results. Figure 20 shows velocity maps derived from standard and modified 3D unwrapping. The comparison between Figure 20a,b shows that modified 3D unwrapping works better especially in areas with high relief.

This is also supported by comparison between ALOS observations and GPS measurements (Figure 16 and Table 1), where we observe an improvement of accuracy of 33% after such correction for ALOS dataset, which is more significant in comparison with 10% improvement for Envisat dataset. The same improvement can be seen from comparison of RMS misclosure related to the three major processing steps. As seen in Figure 18, applying topographic correction within 3D unwrapping reduces unwrapping errors by 70% and 80% for Envisat and ALOS dataset, respectively.

For the available C-band SBAS data, because of their relatively small perpendicular baseline, the sensitivity to topographic changes is decreased, and therefore this correction does not improve the results of the time-series significantly. As a result, for the available Envisat data in this study it would be enough to perform only atmospheric and/or orbit correction during StaMPS processing in order to monitor slow deformation in mountainous regions. This can also be seen in Figure 18a,b in which there is little difference between the red and yellow bars. Comparatively, for the ALOS, this difference is significant as has been illustrated in Figure 18c.

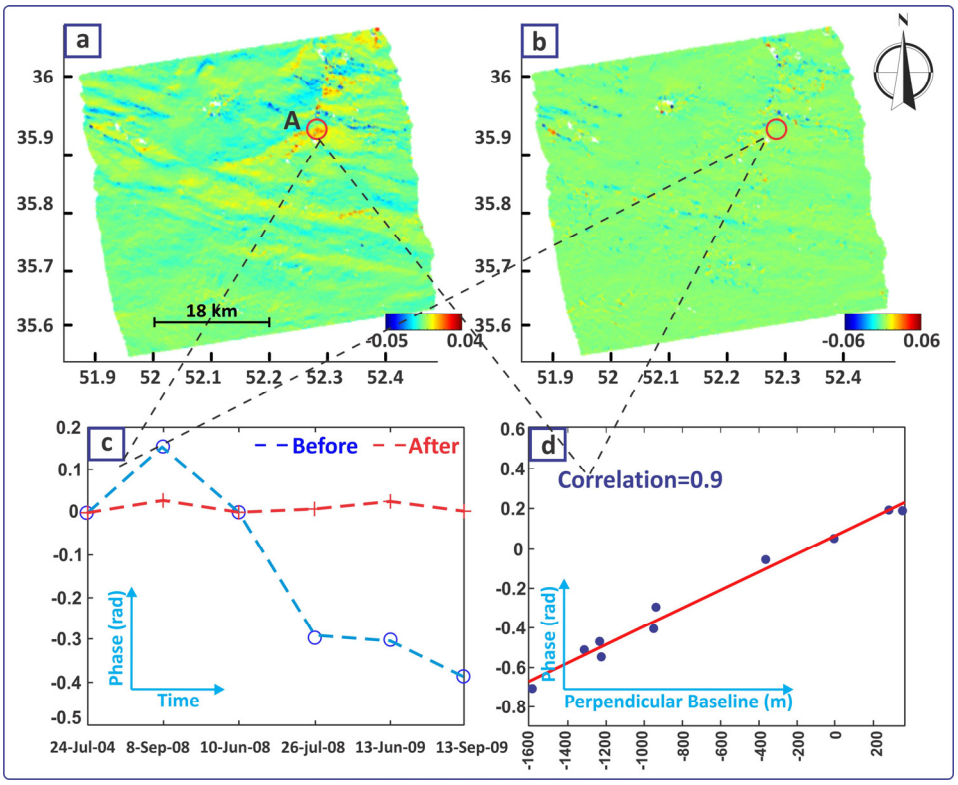

Figure 19. Phase difference map calculated by differencing the phase values between pixels connected by Delaunay edges (a) before and (b) after correction for a pair of ALOS ascending dataset: 24 July 2007 and 13 June 2009; the colorbar is in radian. (**c**) Time series plot for a specific location (point A) before and after applying topographic correction. (**d**) The correlation plot between phase and perpendicular point for point A.

Regarding the third part of correction which is related to atmospheric and orbital correction, our results show that these two corrections improve accuracy up to 70% in the Damavand region (Table 1).

Significant improvement can be seen from a comparison between InSAR observations and GPS measurements, especially for the C-band dataset (Figures 14 and 15), which is more sensitive to atmospheric errors.

Taking into account sensitivity to elevation, atmospheric effect is intensified in elevated areas especially at the top of the Damavand volcano. As seen in Figures 6–9, after applying ISBAS, the correlation between topography and displacement is reduced by 82%. This has an important effect on evaluating the deformation field associated with important geophysical targets in this region. Our observations show an average uplift rate of 3 mm/year around the Damavand summit, which is in agreement with the recent investigation suggesting an inflating magma chamber at depths 3–6 km as the source of deformation at Damavand [56]. Moreover, the active tectonic convergence between the Arabian and Eurasian plates [57,58] partly accommodates in the Alborz Mountains and causes Alborz uplift. In the Damavand region, up to 3 mm/year of uplift has been reported for ABAL station (Figure 4) based on GPS and absolute gravity measurements [50]. Therefore, we suggest that part of the uplift that we observe in the Damavand region might also be related to the overall tectonic uplift in this region.

Table. 1. Root mean square error (RMSE) values between GPS and InSAR results.

RMSE (cm)							
Dataset →	*Envisat descending*	*Envisat Ascending*				*ALOS*	
Processing ↓	PLOR	PLZI	ABSD	ABAL	PLOR	ABAL	PLOR
Stamps	2.2	5.3	6.6	7.5	5.6	4.69	3.9
Atm & Orb correction	0.093	1.3	1.6	1.4	0.67	2.14	1.5
ISBAS	0.66	0.56	1.02	0.87	0.36	0.6	0.4

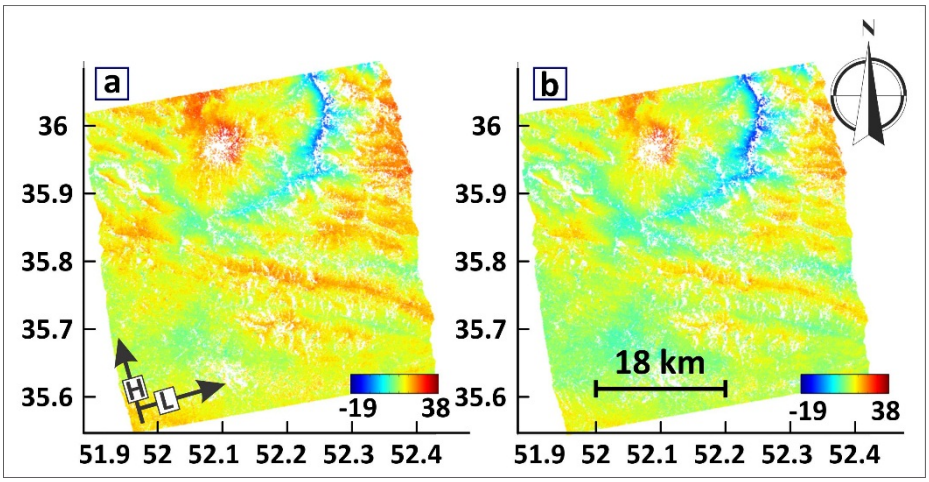

Figure 20. ALOS velocity map before performing atmospheric correction derived from (**a**) standard 3D unwrapping without topographic correction and (**b**) modified 3D unwrapping with topographic correction. The unit of the colorbar is mm/year.

Regarding the interseismic deformation around the Mosha fault, our study supports the left lateral (sinisteral) movements along the fault, which agrees well with previous geological studies [59–64]. It is worth mentioning that the true sense of motion on the Mosha fault can only be observed after performing atmospheric and topographic correction, without which InSAR time-series results would not be interpretable. Inversion of InSAR results shows that the estimated velocity field around the Mosha fault could be well explained by a fault that is locked for about 17–19 km and slips with ~2–4 mm/year below the locking depth. This estimation is in good agreement with the average geological slip rate of 2 ± 0.1 mm/year for the fault [59].

5. Conclusions

In this study, an improved InSAR time-series method was introduced to assess tectonic and volcanic deformation in the center of the Alborz Mountains, Iran. The experiment using Envisat and ALOS data shows that our development dealing with a modified Goldstein filter, topographic correction within the 3D phase unwrapping process, atmospheric and orbit correction helped better characterize tectonic and volcanic deformation signal in the center of the Alborz region than the classical SBAS technique. Comparing with GPS observations, our method shows an improvement in accuracy of the deformation field by up to 75%. Our results demonstrate an uplift signal with the average rate of 3 mm/year on the Damavand volcano. We also derive left-lateral interseismic motion on the Mosha fault that is compatible

with the first order interseismic model in which the fault slips at the rate of ~2–4 mm/year below the locking depth of 17–19 km.

Acknowledgments

Faramarz Nilfouroushan was funded by Swedish Research Council (VR). Envisat and ALOS data were provided by the ESA catergory-1 proposals AOALO3740, AOALO3598 and C1P2892. We thank National Cartographic Center of Iran (NCC) for providing us with GPS observations. We thank Amir Hossein Souri for his help in estimating ZWD from GPS measurements. This study was supported by the Initiative and Networking Fund of the Helmholtz Association in the frame of Helmholtz Alliance "Remote Sensing and Earth System Dynamics."

Author Contributions

Sanaz Vajedian performed the data analysis and wrote the paper with significant contributions from Mahdi Motagh and Faramarz Nilfouroushan for writing the first draft, interpretation of the results and editing the final manuscript.

Conflict of Interest

The authors declare no conflict of interest.

References

1. Motagh, M.; Klotz, J.; Tavakoli, F.; Djamour, Y.; Arabi, S.; Wetzel, H.U.; Zschau, J. Combination of precise leveling and InSAR data to constrain source parameters of the mw = 6.5, 26 December 2003 Bam Earthquake. *Pure Appl. Geophys.* **2006**, *163*, 1–18.
2. Hooper, A.; Bekaert, D.; Spaans, K.; Arikan, M. Recent advances in SAR interferometry time series analysis for measuring crustal deformation. *Tectonophysics* **2012**, *514–517*, 1–13.
3. Caro Cuenca, M.; Hooper, A.J.; Hanssen, R.F. Surface deformation induced by water influx in the abandoned coal mines in Limburg, The Netherlands observed by satellite radar interferometry. *J. Appl. Geophys.* **2013**, *88*, 1–11.
4. Motagh, M.; Schurr, B.; Anderssohn, J.; Cailleau, B.; Walter, T.R.; Wang, R.; Villotte, J.P. Subduction earthquake deformation associated with 14 November 2007, mw 7.8 tocopilla earthquake in Chile: Results from InSAR and aftershocks. *Tectonophysics* **2010**, *490*, 60–68.
5. Motagh, M.; Beavan, J.; Fielding, E.J.; Haghshenas, M. Postseismic ground deformation following the september 2010 darfield, New Zealand, earthquake from TerraSAR-X, COSMO-SkyMed, and ALOS InSAR. *IEEE Geosci. Remote Sens. Lett.* **2014**, *11*, 186–190.
6. Hung, W.C.; Hwang, C.; Chen, Y.A.; Chang, C.P.; Yen, J.Y.; Hooper, A.; Yang, C.Y. Surface deformation from persistent scatterers SAR interferometry and fusion with leveling data: A case study over the Choushui River Alluvial Fan, Taiwan. *Remote Sens. Environ.* **2011**, *115*, 957–967.
7. Li, Z.W.; Xu, W.B.; Feng, G.C.; Hu, J.; Wang, C.C.; Ding, X.L.; Zhu, J.J. Correcting atmospheric effects on InSAR with MERIS water vapour data and elevation-dependent interpolation model. *Geophys. J. Int.* **2012**, *189*, 898–910.

8. Li, Z.; Fielding, E.J.; Cross, P. Integration of InSAR time-series analysis and water-vapor correction for mapping postseismic motion after the 2003 bam (Iran) earthquake. *IEEE Trans. Geosci. Remote Sens.* **2009**, *47*, 3220–3230.
9. Li, Z.; Muller, J.P.; Cross, P.; Fielding, E.J. Interferometric synthetic aperture radar (InSAR) atmospheric correction: GPS, moderate resolution imaging spectroradiometer (MODIS), and InSAR integration. *J. Geophys. Res.: Solid Earth* **2005**, *110*, doi:10.1029/2004JB003446.
10. Fornaro, G.; D'Agostino, N.; Giuliani, R.; Noviello, C.; Reale, D.; Verde, S. Assimilation of GPS-derived atmospheric propagation delay in DInSAR data processing. *IEEE J. Sel. Top. Appl. Earth Obs. Remote Sens.* **2014**, doi:10.1109/JSTARS.2014.2364683.
11. Zebker, H.A.; Villasenor, J. Decorrelation in interferometric radar echoes. *IEEE Trans. Geosci. Remote Sens.* **1992**, *30*, 950–959.
12. Hooper, A.; Segall, P.; Zebker, H. Persistent scatterer interferometric synthetic aperture radar for crustal deformation analysis, with application to Volcán Alcedo, Galápagos. *J. Geophys. Res.: Solid Earth* **2007**, *112*, doi:10.1029/2006JB004763.
13. Hooper, A.J. A multi-temporal InSAR method incorporating both persistent scatterer and small baseline approaches. *Geophys. Res. Lett.* **2008**, *35*, doi:10.1029/2008GL034654.
14. Motagh, M.; Wetzel, H.U.; Roessner, S.; Kaufmann, H. A TerraSAR-X InSAR study of landslides in southern Kyrgyzstan, central Asia. *Remote Sens. Lett.* **2013**, *4*, 657–666.
15. Ferretti, A.; Prati, C.; Rocca, F. Permanent scatterers in SAR interferometry. *IEEE Trans. Geosci. Remote Sens.* **2001**, *39*, 8–20.
16. Ferretti, A.; Savio, G.; Barzaghi, R.; Borghi, A.; Musazzi, S.; Novali, F.; Prati, C.; Rocca, F. Submillimeter accuracy of InSAR time series: Experimental validation. *IEEE Trans. Geosci. Remote Sens.* **2007**, *45*, 1142–1153.
17. Ferretti, A.; Prati, C.; Rocca, F. Nonlinear subsidence rate estimation using permanent scatterers in differential SAR interferometry. *IEEE Trans. Geosci. Remote Sens.* **2000**, *38*, 2202–2212.
18. Kampes, B.M. Displacement Parameter Estimation Using Permanent Scatterer Interferometry. Ph.D. Thesis, Delft University of Technology, Delft, The Netherlands 2005.
19. Hooper, A.; Zebker, H.; Segall, P.; Kampes, B. A new method for measuring deformation on volcanoes and other natural terrains using InSAR persistent scatterers. *Geophys. Res. Lett.* **2004**, *31*, 1–5.
20. Shanker, P.; Zebker, H. Persistent scatterer selection using maximum likelihood estimation. *Geophys. Res. Lett.* **2007**, *34*, doi:10.1029/2007GL030806.
21. Ferretti, A.; Fumagalli, A.; Novali, F.; Prati, C.; Rocca, F.; Rucci, A. A new algorithm for processing interferometric data-stacks: Squeesar. *IEEE Trans. Geosci. Remote Sens.* **2011**, *49*, 3460–3470.
22. Motagh, M.; Hoffmann, J.; Kampes, B.; Baes, M.; Zschau, J. Strain accumulation across the gazikoy-saros segment of the north anatolian fault inferred from persistent scatterer interferometry and GPS measurements. *Earth Planet. Sci. Lett.* **2007**, *255*, 432–444.
23. Berardino, P.; Fornaro, G.; Lanari, R.; Sansosti, E. A new algorithm for surface deformation monitoring based on small baseline differential SAR interferograms. *IEEE Trans. Geosci. Remote Sens.* **2002**, *40*, 2375–2383.

24. Lanari, R.; Casu, F.; Manzo, M.; Zeni, G.; Berardino, P.; Manunta, M.; Pepe, A. An overview of the small baseline subset algorithm: A DInSAR technique for surface deformation analysis. *Pure Appl. Geophys.* **2007**, *164*, 637–661.
25. Lanari, R.; Mora, O.; Manunta, M.; Mallorquí, J.J.; Berardino, P.; Sansosti, E. A small-baseline approach for investigating deformations on full-resolution differential SAR interferograms. *IEEE Trans. Geosci. Remote Sens.* **2004**, *42*, 1377–1386.
26. Lauknes, T.R.; Zebker, H.A.; Larsen, Y. InSAR deformation time series using an-norm small-baseline approach. *IEEE Trans. Geosci. Remote Sens.* **2011**, *49*, 536–546.
27. Schmidt, D.A.; Bürgmann, R. Time-dependent land uplift and subsidence in the santa clara valley, California, from a large interferometric snthetic aperture radar data set. *J. Geophys. Res.: Solid Earth* **2003**, *108*, doi:10.1029/2002JB002267.
28. Jolivet, R.; Grandin, R.; Lasserre, C.; Doin, M.P.; Peltzer, G. Systematic InSAR tropospheric phase delay corrections from global meteorological reanalysis data. *Geophys. Res. Lett.* **2011**, *38*, doi:10.1029/2011GL048757.
29. Fornaro, G.; Reale, D.; Serafino, F. Four-dimensional SAR imaging for height estimation and monitoring of single and double scatterers. *IEEE Trans. Geosci. Remote Sens.* **2009**, *47*, 224–237.
30. Samsonov, S.; Tiampo, K. Time series analysis of subsidence at Tauhara and Ohaaki geothermal fields, New Zealand, observed by ALOS PALSAR interferometry during 2007–2009. *Can. J. Remote Sens.* **2010**, *36*, S327–S334.
31. Fattahi, H.; Amelung, F. Dem error correction in InSAR time series. *IEEE Trans. Geosci. Remote Sens.* **2013**, *51*, 4249–4259.
32. Samsonov, S. Topographic correction for ALOS PALSAR interferometry. *IEEE Trans. Geosci. Remote Sens.* **2010**, *48*, 3020–3027.
33. Pinel, V.; Hooper, A.; de la Cruz-Reyna, S.; Reyes-Davila, G.; Doin, M.P.; Bascou, P. The challenging retrieval of the displacement field from InSAR data for andesitic stratovolcanoes: Case study of Popocatepetl and Colima Volcano, Mexico. *J. Volcanol. Geotherm. Res.* **2011**, *200*, 49–61.
34. Hooper, A.J. Persistent Scatter Radar Interferometry for Crustal Deformation Studies and Modeling of Volcanic Deformation. Ph.D. Thesis, Stanford University, Stanford, CA, USA, 2006.
35. Hooper, A.; Zebker, H.A. Phase unwrapping in three dimensions with application to InSAR time series. *J. Opt. Soc. Am. A: Opt. Image Sci. Vis.* **2007**, *24*, 2737–2747.
36. Hooper, A. Bayesian inversion of wrapped InSAR data for geophysical parameter estimation. In Proceedings of ESA Living Planet Symposium, Bergen, Norway, 28 June–2 July 2010.
37. Goldstein, R.M.; Werner, C.L. Radar interferogram filtering for geophysical applications. *Geophys. Res. Lett.* **1998**, *25*, 4035–4038.
38. Baran, I.; Stewart, M.P.; Kampes, B.M.; Perski, Z.; Lilly, P. A modification to the goldstein radar interferogram filter. *IEEE Trans. Geosci. Remote Sens.* **2003**, *41*, 2114–2118.
39. Doin, M.P.; Lasserre, C.; Peltzer, G.; Cavalié, O.; Doubre, C. Corrections of stratified tropospheric delays in SAR interferometry: Validation with global atmospheric models. *J. Appl. Geophys.* **2009**, *69*, 35–50.
40. Pinel, V.; Hooper, A.; de la Cruz-Reyna, S.; Reyes-Davila, G.; Doin, M.P. *Study of the Deformation Field of Two Active Mexican Stratovolcanoes (Popocatepetl and Colima Volcano) by Time Series of Insar Data*; European Space Agency: Paris, France, 2008.

41. Emardson, T.R.; Johansson, J.M. Spatial interpolation of the atmospheric water vapor content between sites in a ground-based GPS network. *Geophys. Res. Lett.* **1998**, *25*, 3347–3350.
42. Li, Z.; Fielding, E.J.; Cross, P.; Muller, J.P. Interferometric synthetic aperture radar atmospheric correction: GPS topography-dependent turbulence model. *J. Geophys. Res.: Solid Earth* **2006**, *111*, doi:10.1029/2005JB003711.
43. Li, Z.; Ding, X.; Huang, C.; Wadge, G.; Zheng, D. Modeling of atmospheric effects on InSAR measurements by incorporating terrain elevation information. *J. Atmos. Sol. Terr.Phys.* **2006**, *68*, 1189–1194.
44. Xu, W.; Li, Z.; Ding, X.; Zhu, J. Interpolating atmospheric water vapor delay by incorporating terrain elevation information. *J. Geod.* **2011**, *85*, 555–564.
45. Onn, F.; Zebker, H. Correction for interferometric synthetic aperture radar atmospheric phase artifacts using time series of zenith wet delay observations from a GPS network. *J. Geophys. Res. Solid Earth* **2006**, *111*, doi:10.1029/2005JB004012.
46. Zumberge, J.; Heflin, M.; Jefferson, D.; Watkins, M.; Webb, F.H. Precise point positioning for the efficient and robust analysis of GPS data from large networks. *J. Geophys. Res.: Solid Earth* **1997**, *102*, 5005–5017.
47. Sharifi, M.; Souri, A. A hybrid LS-HE and LS-SVM model to predict time series of precipitable water vapor derived from GPS measurements. *Arabian J. Geosci.* **2014**, doi:10.1007/s12517-014-1716-0.
48. Agram, P.S. Persistent Scatterer Interferometry in Natural Terrain. Ph.D. Thesis, Stanford University, Stanford, CA, USA, 2010.
49. Samieie-Esfahany, S.; Hanssen, R.; van Thienen-Visser, K.; Muntendam-Bos, A. On the effect of horizontal deformation on InSAR subsidence estimates. In Proceedings of the Fringe 2009 Workshop, Frascati, Italy, 30 November–4 December 2009.
50. Djamour, Y.; Vernant, P.; Bayer, R.; Nankali, H.R.; Ritz, J.; Hinderer, J.; Hatam, Y.; Luck, B.; Le Moigne, N.; Sedighi, M.; *et al.* GPS and gravity constraints on continental deformation in the Alborz Mountain Range, Iran. *Geophys. J. Int.* **2010**, *183*, 1287–1301.
51. Savage, J.; Burford, R. Accumulation of tectonic strain in California. *Bull. Seismol. Soc. Am.* **1970**, *60*, 1877–1896.
52. Haupt, R.L.; Haupt, S.E. *Practical Genetic Algorithms*; John Wiley & Sons: Hoboken, NJ, USA, 2004.
53. Cressie, N. *Statistics for Spatial Data: Wiley Series in Probability and Statistics*; Wiley-Interscience: Hoboken, NJ, USA, 1993.
54. Mora, O.; Mallorqui, J.J.; Broquetas, A. Linear and nonlinear terrain deformation maps from a reduced set of interferometric SAR images. *IEEE Trans. Geosci. Remote Sens.* **2003**, *41*, 2243–2253.
55. Biescas, E.; Crosetto, M.; Agudo, M.; Monserrat, O.; Crippa, B. Two radar interferometric approaches to monitor slow and fast land deformation. *J. Surv. Eng.* **2007**, *133*, 66–71.
56. Yazdanparast, M.; Vosooghi, B. A research on damavand magma source model using GPS data. *Geomat. Nat. Hazards Risk* **2014**, *5*, 26–40.
57. Nilforoushan, F.; Masson, F.; Vernant, P.; Vigny, C.; Martinod, J.; Abbassi, M.; Nankali, H.; Hatzfeld, D.; Bayer, R.; Tavakoli, F.; *et al.* GPS network monitors the Arabia-Eurasia collision deformation in Iran. *J. Geod.* **2003**, *77*, 411–422.

58. Vernant, P.; Nilforoushan, F.; Chéry, J.; Bayer, R.; Djamour, Y.; Masson, F.; Nankali, H.; Ritz, J.F.; Sedighi, M.; Tavakoli, F. Deciphering oblique shortening of central Alborz in Iran using geodetic data. *Earth Planet. Sci. Lett.* **2004**, *223*, 177–185.
59. Ritz, J.; Balescu, S.; Soleymani, S.; Abbassi, M.; Nazari, H.; Feghhi, K.; Shabanian, E.; Tabassi, H.; Farbod, Y.; Lamothe, M. Determining the long-term slip rate along the Mosha Fault, Central Alborz, Iran. Implications in terms of seismic activity. In Proceeding of the 4th International Conference on Seismology and Earthquake Engeneering, Tehran, Iran, 12–14 May 2003.
60. Peyret, M.; Djamour, Y.; Rizza, M.; Ritz, J.F.; Hurtrez, J.E.; Goudarzi, M.A.; Nankali, H.; Chéry, J.; le Dortz, K.; Uri, F. Monitoring of the large slow kahrod landslide in Alborz Mountain Range (Iran) by GPS and SAR interferometry. *Eng. Geol.* **2008**, *100*, 131–141.
61. Allen, M.B.; Ghassemi, M.R.; Shahrabi, M.; Qorashi, M. Accommodation of late cenozoic oblique shortening in the Alborz Range, northern Iran. *J. Struct. Geol.* **2003**, *25*, 659–672.
62. Zanchi, A.; Berra, F.; Mattei, M.; Ghassemi, M.R.; Sabouri, J. Inversion tectonics in central Alborz, Iran. *J. Struct. Geol.* **2006**, *28*, 2023–2037.
63. Yassaghi, A.; Madanipour, S. Influence of a transverse basement fault on along-strike variations in the geometry of an inverted normal fault: Case study of the mosha fault, central Alborz Range, Iran. *J. Struct. Geol.* **2008**, *30*, 1507–1519.
64. Ashtari, M.; Hatzfeld, D.; Kamalian, N. Microseismicity in the region of tehran. *Tectonophysics* **2005**, *395*, 193–208.